

High-pressure synthesis and sequential ferrimagnetic ordering and spin glass transition of an Fe/Ru disordered quadruple perovskite $CeCu_3Fe_2Ru_2O_{12}$

Sumei Li(李素梅), Gaochao Zhao(赵高超), Meng Wang(王萌), Lihua Yin(尹利华), Peng Tong(童鹏), Xuebin Zhu(朱雪斌), Jie Yang(杨杰), and Yuping Sun(孙玉平)

Citation: Chin. Phys. B, 2026, 35 (**4**): 048103. DOI: 10.1088/1674-1056/ae0399
http://cpb.iphy.ac.cn; http://iopscience.iop.org/cpb

What follows is a list of articles you may be interested in

The B-site ordering in $RFe_{0.5}Cr_{0.5}O_3$ ceramics and its effect on magnetic properties

Li Hou(侯利), Lei Shi(石磊), Liping Yang(杨利平), Yiqiang Liu(刘义强), Zhitao Li(李志涛), and Lanxiang Meng(孟蓝翔)

Chin. Phys. B, 2024, 33 (**10**): 108101. DOI: 10.1088/1674-1056/ad641e

Effect of antioxidants on the efficiency of jet milling and the powder characteristics of Sm_2Co_{17} permanent magnets

Da-Shuai Xu(许大帅), Lei Liu(刘雷), Jian-Hui Yuan(袁建辉), Bo Zhou(周波), Chuang-Hui Dong(董创辉), Feng-Qing Wang(王凤青), Yong Ding(丁勇), Ying-Li Sun(孙颖莉), and A-Ru Yan(闫阿儒)

Chin. Phys. B, 2024, 33 (**9**): 098103. DOI: 10.1088/1674-1056/ad5537

Effects of Cu and Co additions on the crystallization and magnetic properties of FeNbB alloy

Wan-Qiu Yu(于万秋), Bo Tian(田博), Ping-Li Zhang(张平丽), Jia-Hui Wang(王佳慧), and Zhong Hua(华中)

Chin. Phys. B, 2023, 32 (**8**): 088102. DOI: 10.1088/1674-1056/acd525

Low temperature ferromagnetism in $CaCu_3Ti_4O_{12}$

Song Yang(杨松), Xiao-Jing Luo(罗晓婧), Zhi-Ming Shen(申志明), Tian Gao(高湉), Yong-Sheng Liu(刘永生), and Shao-Long Tang(唐少龙)

Chin. Phys. B, 2021, 30 (**9**): 098103. DOI: 10.1088/1674-1056/abeef0

A-site ordered quadruple perovskite oxides $AA_3'B_4O_{12}$

Youwen Long(龙有文)

Chin. Phys. B, 2016, 25 (**7**): 078108. DOI: 10.1088/1674-1056/25/7/078108

High-pressure synthesis and sequential ferrimagnetic ordering and spin glass transition of an Fe/Ru disordered quadruple perovskite $CeCu_3Fe_2Ru_2O_{12}$

Sumei Li(李素梅)[1,2], Gaochao Zhao(赵高超)[1,2], Meng Wang(王萌)[1,2], Lihua Yin(尹利华)[1], Peng Tong(童鹏)[1], Xuebin Zhu(朱雪斌)[1], Jie Yang(杨杰)[1,†], and Yuping Sun(孙玉平)[1,3,4]

[1] *Institute of Solid State Physics, Chinese Academy of Sciences, Hefei* 230031, *China*
[2] *University of Science and Technology of China, Hefei* 230026, *China*
[3] *High Magnetic Field Laboratory, Chinese Academy of Sciences, Hefei* 230031, *China*
[4] *Collaborative Innovation Center of Advanced Microstructures, Nanjing University, Nanjing* 210093, *China*

(Received 7 July 2025; revised manuscript received 21 August 2025; accepted manuscript online 5 September 2025)

We successfully prepared an *A*-site-ordered quadruple perovskite oxide $CeCu_3Fe_2Ru_2O_{12}$ by using a high-pressure method (10 GPa, 1400 K). The compound crystallizes in the $Im\bar{3}$ space group, with *A*-site ordering of Ce and Cu ions in a ratio of 1:3, but *B*-site disordered distribution of Fe and Ru ions. Bond-value-sum calculations and x-ray photoelectron spectroscopy measurement manifest that the charge distribution is $Ce^{3.5+}Cu_3^{2+}Fe_2^{3+}Ru_2^{4.25+}O_{12}$. A ferrimagnetic phase transition occurs at $T_C = 73.6$ K followed by a spin glass behavior at 50.3 K consistent with the conventional dynamical scaling power law. Electrical transport measurement shows that the intrinsic electrical behavior is semiconducting and the resistivity obey the adiabatic small-polaron model. The specific heat follows a T^2 law instead of traditional phonon-dominated T^3 behavior implying a finite energy gap in the excitation spectrum.

Keywords: *A*-site ordered perovskite, high pressure synthesis, magnetic properties

PACS: 81.40.Vw, 75.30.–m, 75.47.Lx

DOI: 10.1088/1674-1056/ae0399 **CSTR:** 32038.14.CPB.ae0399

1. Introduction

Benefiting from the development of high-pressure instruments, researchers are increasingly interested in the *A*-site-ordered quadruple perovskite oxide with stoichiometry $AA'_3B_4O_{12}$. In this system, the *A* site is usually filled with alkaline metal, alkaline-earth metal, or earth metal ions. The A' site is typically occupied by Jahn–Teller ions, such as Cu^{2+} and Mn^{3+}. Meanwhile, the *B* site is also occupied by transition metal ions. To sustain the structural stability, the co-angled BO_6 octahedron is heavily tilted, resulting in square-coordinated $A'O_4$ units being arranged perpendicularly to each other.[1] The presence of two different transition-metal ions at the A' and *B* sites gives rise to multiple interactions, including A'–A', A'–*B*, and *B*–*B* interactions. The charges, spins, orbitals, and lattices are coupled. This coupling leads to the observation of intriguing properties in $AA'_3B_4O_{12}$,[2] such as multiferroicity,[3,4] intermetallic charge transfer,[5–9] catalyst,[10] charge disproportionation,[11–13] colossal magnetoresistance,[14,15] giant dielectric constant,[16,17] negative thermal expansion,[6,7,18,19] and d-electron heavy fermion state.[20,21]

The valence state of transition-metal (TM) cations plays an important role in the chemical and physical properties of compounds. Chemical substitution, including ectopic and isotope doping, is used to introduce electron doping into transition-metal ions. For instance, $CaCu_3Fe_4O_{12}$ exhibits a charge disproportionation transition $2Fe^{4+} \rightarrow Fe^{3+}+Fe^{5+}$ with a rock-salt-type Fe^{3+}:Fe^{5+}. This transition is accompanied by ferrimagnetic, metal-semiconductor and $Im\bar{3}$ to $Pn\bar{3}$ structural transition below 210 K.[8,11] In contrast, electron doping into $LaCu_3Fe_4O_{12}$ leads to an intersite charge transfer transition $3Cu^{2+}+4Fe^{3.75+} \rightarrow 3Cu^{3+}+4Fe^{3+}$, accompanied by G-type antiferromagnetic, metal–insulator transition, and negative thermal expansion below 393 K.[8] When Ca^{2+} is substituted by Y^{3+}, $YCu_3Fe_4O_{12}$ exhibits similar properties, including a charge disproportionation transition $8Fe^{3.75+} \rightarrow 3Fe^{5+}+5Fe^{3+}$ and other transition below 250 K.[13] These structural and electronic phase transitions are ascribable to bond strain. In the $AA'_3B_2B'_2O_{12}$ compounds, sequential electron doping in $Na/Ca/LaCu_3Fe_2Os_2O_{12}$ does not change the magnetic interaction of Cu(↑)Fe(↓)Os(↓), but enhances the ferrimagnetic transition temperature (from 380 K to 580 K to 520 K) and worsens electrical conductivity (from half-metal to semiconductor to insulator).[22–24] $CaCu_3Fe_2Re_2O_{12}$ is a ferrimagnetic half metal owing to Cu(↑)Fe(↓)Re(↓) spin coupling. $LaCu_3Fe_2Re_2O_{12}$ only increases the Curie temperature up to 710 K.[25,26] In particular, two magnetic phase transitions occur in the insulator $CaCu_3Co_2Re_2O_{12}$ with an energy gap (E_{gap}) of 3.75 eV. The antiferromagnetic phase transition occurs at 28 K arising from the $A'(Cu^{2+}(\uparrow))$–

†Corresponding author. E-mail: jyang@issp.ac.cn

© 2026 Chinese Physical Society and IOP Publishing Ltd. All rights, including for text and data mining, AI training, and similar technologies, are reserved.

$A'(Cu^{2+}(\downarrow))$ antiferromagnetic interaction. Then the ferrimagnetic phase transition occurs near 20 K resulting from the $B(Co^{2+}(\uparrow))$–$B'(Re^{6+}(\downarrow))$ coupling.[27] On the contrary, only one magnetic phase transition is observed around 150 K in half-metallicity $LaCu_3Co_2Re_2O_{12}$ because of the $Cu^{2+}(\uparrow)$–$Co^{2+}(\uparrow)$–$Re^{5.5+}(\downarrow)$ spin interaction.[28]

In this work, we have successfully prepared and investigated a novel *A*-site-ordered quadruple perovskite oxide $CeCu_3Fe_2Ru_2O_{12}$. A ferrimagnetic phase transition is observed at $T_C = 73.6$ K and subsequently a spin glass behavior occurs around $T_{SG} = 50.3$ K. The low temperature heat capacity deviates significantly from the typical phonon-dominated T^3 law, but obeys the T^2 relationship.

2. Experimental details

$CeCu_3Fe_2Ru_2O_{12}$ (CeCFRO) bulk sample was prepared under high-temperature and high-pressure conditions. CeO_2 (99.99%), CuO (99%), Fe_2O_3 (99.8%), and RuO_2 (99.99%) in stoichiometric amounts were fully mixed and grounded with a proper amount oxidizing agent $KClO_4$. The well-mixed reagents were encapsulated by a platinum capsule, then heated at 1400 K and 10 GPa for 1 h using a Walker-type multi-anvil apparatus. After the heating process was finished, the sample was quenched immediately, and then the pressure was slowly released to ambient conditions. Powder x-ray diffraction (PXRD) was carried out with a Philips X'pert PRO x-ray diffractometer using Cu K_α radiation to determine the sample quality and crystal structure. X-ray photoelectron spectroscopy (XPS) measurement was performed with a Thermo ESCALAB 250Xi using monochromatic Al K_α source ($P =$ 150 W, $h\nu = 1486.6$ eV). The magnetic measurements were carried out with a Quantum Design (QD) superconducting quantum interference device (SQUID) and a magnetic property measurement system (MPMS) ($5\ \text{K} \leq T \leq 380\ \text{K}$, $0 \leq H \leq 45$ kOe, 1 Oe = 79.5775 A·m^{-1}). Electrical resistivity which was using the four-probe method and specific heat were measured by QD physical property measurement system (PPMS).

3. Results and discussion

Figure 1(a) shows the PXRD pattern at room temperature (RT) and the corresponding Rietveld refinement of CeCFRO. There is no detectable impurity phase. The compound exhibits *A*-siteordered perovskite structure with the $Im\bar{3}$ space group. For the $AA'_3B_2B'_2O_{12}$ compounds, the presences of characteristic reflections with indices satisfying $h+k+l =$ odd, *e.g.*, (111), (311), and (331) serves as a criterion for rocksalt-type ordering of *B*-site ions. The absence of these characteristic peaks in CeCFRO reveals disordered Fe and Ru ions occupying the *B* sites (inset of Fig. 1(a)), which is similar to $CaCu_3Cr_2Ru_2O_{12}$.[29] The refined structure parameters of CeCFRO are summarized in Table 1. The valence state of ion was calculated using the bond valence sum (BVS) method with the relation: $V_i = \sum_i^n \exp((r_0 - r_i)/B)$, where n is the number of bonds, r_0 is the relevant bond length, r_i is the bond length, and B is a constant ($B = 0.37$ Å).[30] The tentative calculated BVS of Ce using $r_0(Ce^{3+}) = 2.151$ Å, $r_0(Ce^{4+}) =$ 2.028 Å, and $r_0(Ce^{n+}) = 2.094$ Å,[31] yielded BVS values of +4.07, +3.25, and +3.49, respectively, implying the mixed valence state of Ce ions. Similarly, Cu exhibits a BVS of +1.94, consistent with a purely divalent state in the CuO_4-square (Table 1). The BVS method is not suitable to obtain the reliable valence states of Fe and Ru ions because of random distribution of these ions at the *B*-sites.

Table 1. Structure parameters and BVS results of CeCFRO refined from XRD pattern at room-temperature. Space group $Im\bar{3}$. Atomic sites: Ce 2*a* (0, 0, 0), Cu 6*b* (0, 0.5, 0.5), Fe/Ru 8*c* (0.25, 0.25, 0.25), O 24*g* (0, 0.1672(2), 0.2990(1)). The BVS values (V_i) were calculated using the formula $V_i = \sum_j S_{ij}$, where $S_{ij} = \exp[(r_0 - r_{ij})/0.37)]$, $r_0(Ce^{3+}) = 2.151$ Å, $r_0(Ce^{4+}) = 2.028$ Å, $r_0(Ce^{n+}) = 2.094$ Å, and $r_0(Cu^{2+}) = 1.679$ Å.

Parameter	CeCFRO
a (Å)	7.4455(9)
V (Å^3)	412.7597(6)
Ce–O (×4) (Å)	2.5507(8)
Cu–O (×4) (Å)	1.9467(4)
$\angle B/B'$–O–B/B' (°)	137.9(1)
$\angle$Cu–O–B/B' (°)	109.7(7)
BVS (Ce^{3+})	4.07(3)
BVS (Ce^{4+})	3.25(5)
BVS (Ce^{n+})	3.49(2)
BVS (Cu)	1.94(4)

To further confirm the valence states of Ce, Cu, Fe, and Ru ions in CeCFRO, XPS was measured. As shown in Fig. 1(b), the Ce 3d core-level spectrum shows a characteristic peak near 916 eV corresponding to the characteristic peak of Ce^{4+}.[32,33] Peak deconvolution of Ce 3d spectrum reveals two characteristic peaks corresponding to Ce^{3+} and Ce^{4+}. The semi-quantitative calculation of the integral peak area yields approximately 50% Ce^{4+} content, consistent with the theoretical calculation results of BVS. In Fig. 1(c), the oxidation states of Cu^{2+} are confirmed by two main peaks at 934.33 eV (Cu $2p_{3/2}$) and 954.22 eV (Cu $2p_{1/2}$), accompanied by three satellite peaks at 941.65 eV, 944.15 eV, and 962.49 eV.[33,34] In Fig. 1(d), peak resolution of the Ru $3p_{3/2}$ spectra resolves a bimodal structure: the peak with higher binding energy corresponds to Ru^{5+}, while the peak with lower binding energy is related to Ru^{4+}.[35] The content ratio of Ru^{4+}:Ru^{5+} is about 3:1 according to peak area integration. It is difficult to accurately determine the valence state of Fe 2p by conventional XPS peak fitting method because of the serious spectral broadening. According to the principle of charge neutralization and the valence state distribution characteristics of these isomorphic compounds $ACu_3Fe_2B'_2O_{12}$ (A = Na, Ca, La, B' = Sb, Nb, Ta, Os, Re),[22–26,36–38] it can be reasonably inferred that the valence state of Fe ion should be +3. Hence the charge configuration is proposed as $Ce^{3.5+}Cu_3^{2+}Fe_2^{3+}Ru_2^{4.25+}O_{12}$.

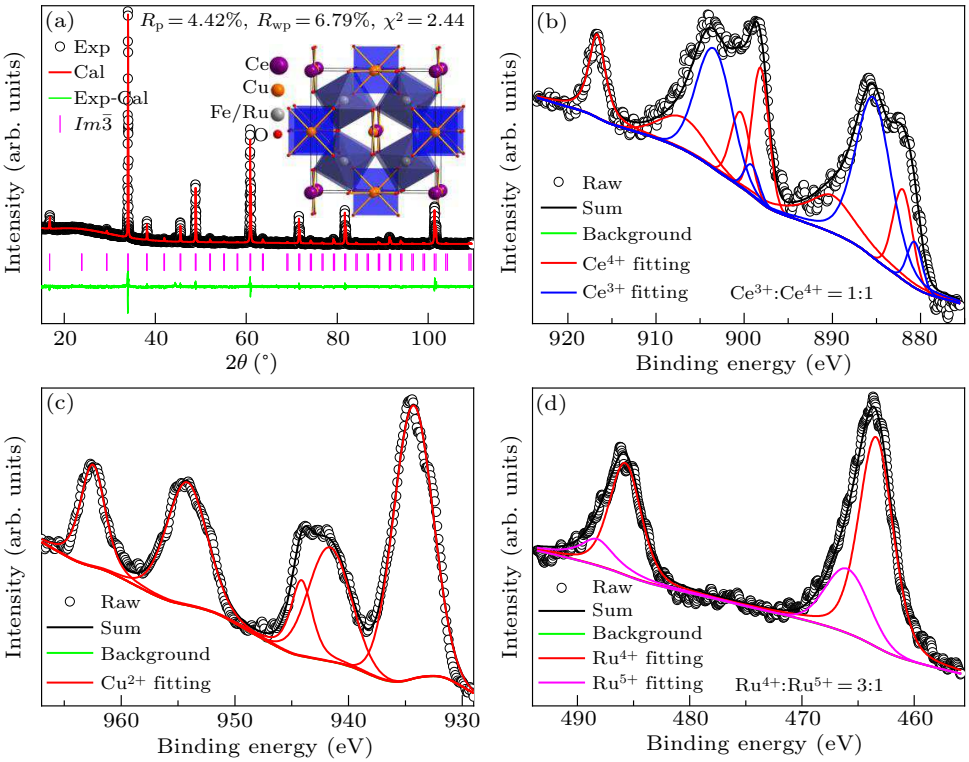


Fig. 1. (a) XRD pattern and structure refinement results of $CeCu_3Fe_2Ru_2O_{12}$ at room temperature. The observed (black circles), calculated (red line), and difference (green line) patterns are shown. The tick marks show possible Bragg reflection positions with space group $Im\bar{3}$. The inset shows schematic crystal structure for $CeCu_3Fe_2Ru_2O_{12}$. XPS core-level spectra of (b) Ce 3d, (c) Cu 2p, and (d) Ru 3p for $CeCu_3Fe_2Ru_2O_{12}$, and the fitting curves.

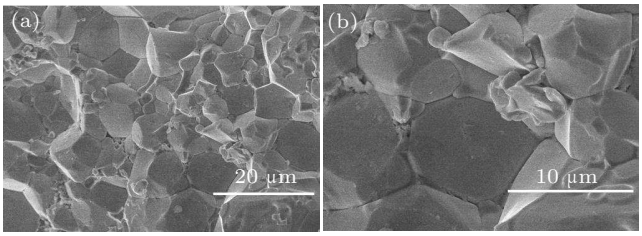


Fig. 2. SEM images of $CeCu_3Fe_2Ru_2O_{12}$ at (a) 20 μm and (b) 10 μm scales.

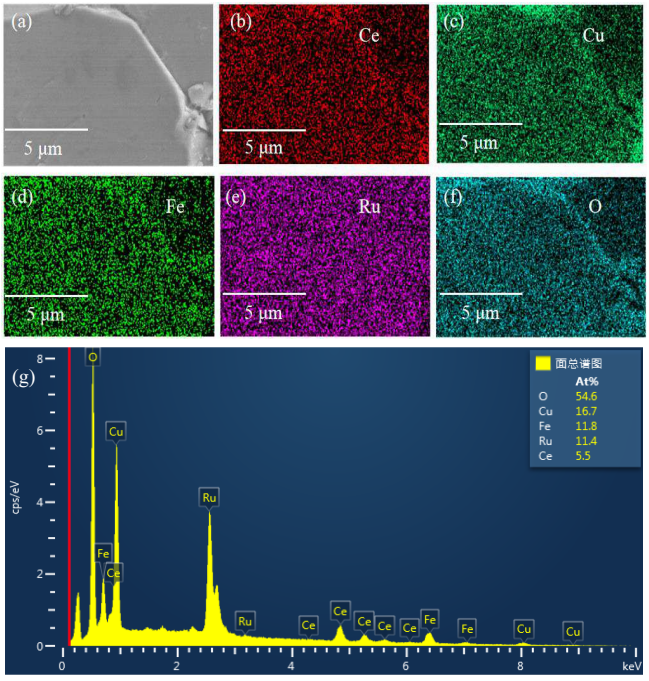


Fig. 3. (a)–(g) EDS spectra of $CeCu_3Fe_2Ru_2O_{12}$.

The microstructure of CeCFRO was characterized using scanning electron microscopy (SEM). As shown in Figs. 2(a) and 2(b), the sample exhibits low intergranular porosity and high densification. The energy-dispersive x-ray spectroscopy (EDS) mapping (Figs. 3(a)–3(g)) confirms uniform distribution of various elements. Quantitative EDS analysis reveals a molar ratio of Ce:Cu:Fe:Ru:O = 1:3.04:2.15:2.07:9.93, deviating significantly from the ideal stoichiometry of oxygen. This discrepancy implies the presence of oxygen vacancies in CeCFRO.

Figure 4(a) depicts the temperature dependence of magnetization measured at different applied magnetic fields for CeCFRO using zero-field-cooled (ZFC), field cooled with data collected on cooling (FCC), and field cooled with data collected on warming (FCW) modes. Upon cooling, the ZFC magnetization (M_{ZFC}) undergoes an abrupt upturn at 73.6 K, indicting a ferromagnetic (FM) or ferrimagnetic (FiM) transition. A secondary anomaly at around $T_{SG} = 50.29$ K (corresponding to the M_{ZFC} peak maximum) is observed, which is later confirmed as spin glass behavior through ac magnetization measurements. Moreover, increasing the applied magnetic field broadens the cusp in M_{ZFC}, shifts its position to lower temperatures, and causes M_{ZFC} and M_{FCC} to converge, accompanied by gradual intensity enhancement.[39] These features are hallmark signatures of spin glass behavior. The temperature dependence of reciprocal magnetic susceptibility ($1/\chi = H/M$) in the paramagnetic region (inset of Fig. 4(a)) obeys the empirical relation:[40] $1/\chi_0 = 1/\chi_0 +$

$T/C_m - \sigma/(T-\theta)$ in the paramagnetic region, where χ_0, C_m, σ, and θ are fitting parameters.[41] This typical hyperbolic behavior implies that CeCFRO undergoes the FiM phase transition at 73.6 K. The fit yields $1/\chi_0 = 46.898 \pm 0.146$ mol/emu, $C_m = 20.154 \pm 0.151$ emu·K/mol, $\sigma = 78.00 \pm 0.23$ K, $\theta = 744.577 \pm 9.108$ mol·K/emu. The experimental effective magnetic moment was calculated as $\mu_{eff} = 12.65\ \mu_B$/f.u. using the relation , where k_B, N, C_m, Z represent Boltzmann's constant, Avogadro's number, the molar Curie constant, and the number of formula units per unit cell, respectively. Additionally, the expected effective moment for one type of magnetic ions is given by, where x is the fraction of magnetic ions per formula unit, g is the gyromagnetic factor, and S is their spin quantum number. CeCFRO contains magnetic ions of Ce^{3+}, Cu^{2+}, Fe^{3+}, Ru^{4+}, and Ru^{5+}. According to the XPS result, the ratio of Ce^{3+}:Ce^{4+} is about 1:1, and Ru^{4+}:Ru^{5+} is about 3:1. The theoretical effective moment can be calculated from the relation: $\sum \sqrt{\mu_{effi}^2} = g\sqrt{x_1 S_i(S_i+1)}$ using the following parameters: Ce^{3+} ions of $x_1 = 0.5$ and $S_1 = 1/2$, Cu^{2+} ions $x_2 = 3$ and $S_2 = 1/2$, Fe^{3+} ions of $x_3 = 2$ and $S_3 = 3/2$, Ru^{4+} ions of $x_4 = 1.5$, and Ru^{5+} ions of $x_5 = 0.5$ and $S_5 = 3/2$. It is noted that Ru^{4+} exhibits three spin sates of $S = 0$, $S = 1$, and $S = 2$. Therefore, the expected effective moments yield 9.31, 9.94, and 11.71 μ_B/f.u., respectively. The calculated value 11.71 μ_B/f.u. is closer to the experimental date (12.65 μ_B/f.u.), suggesting Ru^{4+} exists in the form of high spin state with $S = 2$.

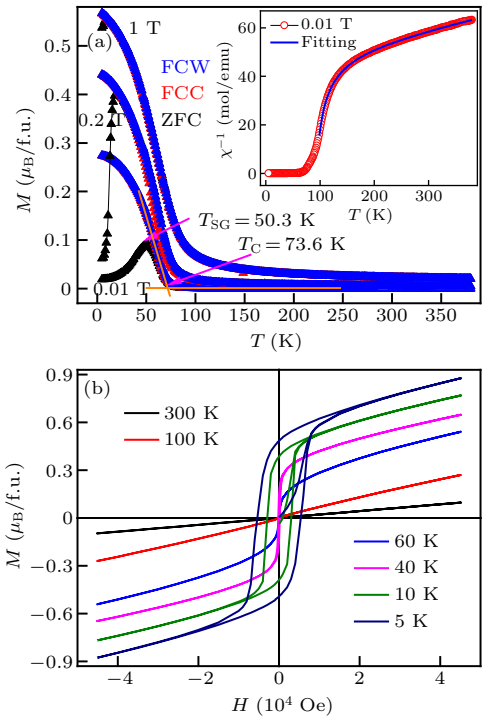


Fig. 4. (a) Magnetization of $CeCu_3Fe_2Ru_2O_{12}$ measured at the magnetic field of 0.01 T, 0.2 T, and 1 T. The inset shows that the inverse susceptibility and the Curie–Weiss fitting. (b) M–H hysteresis loop measured at selected temperature.

Figure 4(c) shows the field-dependent magnetization at selected temperatures. The M–H curves show typical paramagnetic (PM) behavior above 100 K, whereas ferromagnetic-like behavior at other temperature. At 5 K, pronounced hysteresis with coercive field $H_C = 5000$ Oe and unsaturated magnetization up to 4.5 T are observed.

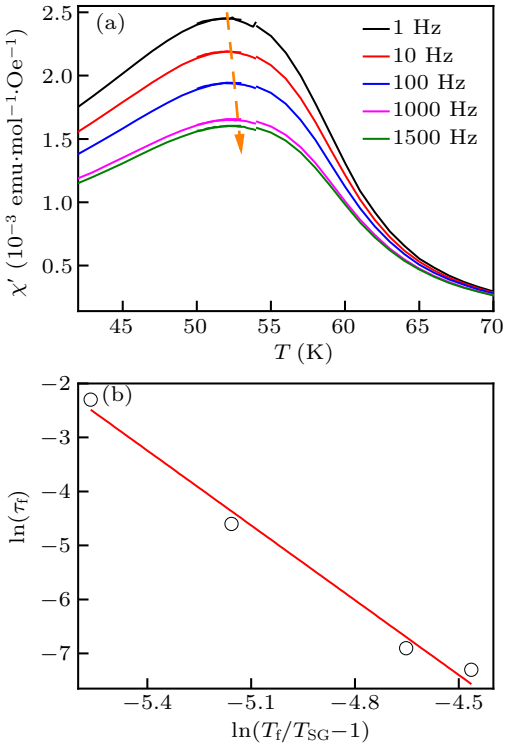


Fig. 5. (a) Temperature dependence of ac magnetic susceptibility measured at different frequencies for $CeCu_3Fe_2Ru_2O_{12}$. (b) The plot of $\ln(\tau_f)$ versus $\ln(T_f/T_{SG}-1)$ and the fitting line.

The ac magnetic susceptibility (χ'_{ac}) curves provide critical evidence for identifying glassy systems. Figure 5(a) shows χ'_{ac} data measured at various frequencies under an applied field of 2 Oe. A broad peak emerges at the spin freezing temperature T_f. which shifts slightly toward higher temperatures and decreases in intensity with increasing frequency. These features are characteristics of spin glass or superparamagnetic systems. To distinguish these two states, we use the Mydosh parameter analysis:[42,43] $\kappa = \Delta T_f/[T_f \Delta \ln(f)]$, where T_f is the spin freezing temperature, f is the frequency, $\Delta T_f = (T_{f1} - T_{f2})$, and $\Delta \ln(f) = \ln f_1 - \ln f_2$. The calculated κ value of 0.0016 falls far below the superparamagnetic range (0.1–0.3),[43,44] but aligns with the spin glass range (10^{-3}–10^{-2}), confirming the glassy behavior of CeCFRO at low temperatures. Moreover, the dynamic deceleration model relates T_f to the fluctuation time scale $\tau = 1/(2\pi f)$ by the relation: $\tau_0/\tau = [(T_f - T_g)/T_g]^{-zv}$, where T_g is the ordering temperature as f tends to 0, τ_0 is the intrinsic relaxation time, and zv is the dynamic exponent.[45] Figure 5(b) shows the curve and fitting results of τ_f and T_f, yielding $zv = 4.62 \pm 0.37$ and $\tau_0 = 9.11 \times 10^{-13}$ s. The value of zv lies within the typical range of 4–12 reported for spin glasses. The value of τ_0 matches the classical spin glasses (10^{-12} s–10^{-13} s), distinct

from cluster spin glasses (10^{-7} s–10^{-10} s). Obviously, the parameters of zv and τ_0 are in good agreement with the classical spin glasses and the isomorphic compound $CaCu_3Mn_2Ir_2O_{12}$ ($zv = 5.1$, $\tau_0 = 2.6 \times 10^{-13}$ s),[46] further confirming the formation of a spin glass state in CeCFRO.

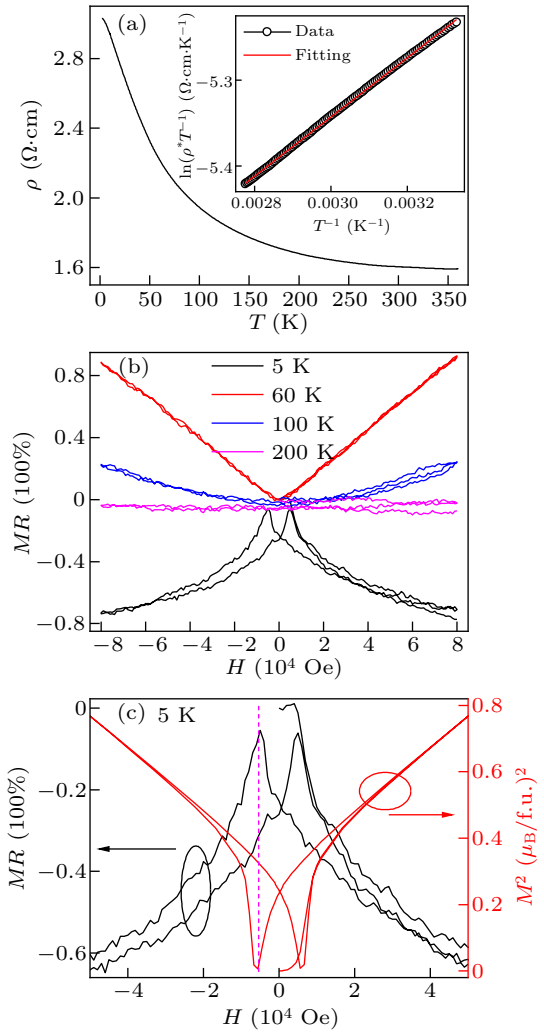


Fig. 6. (a) Temperature dependence of resistivity of $CeCu_3Fe_2Ru_2O_{12}$. The inset shows the fitting result by the adiabatic small-polaron model between 300 K and 360 K. (b) Magnetoresistance as a function of magnetic field measured at different temperatures. (c) Magnetic field dependence of MR and M^2 at 5 K.

To investigate the electrical transport properties of CeCFRO, resistivity and magnetoresistance (MR) were measured. As shown in Fig. 6(a), the compound exhibits semiconducting behavior with resistivity increasing monotonically with the decrease of temperature. In the inset of Fig. 6(a), the ρ–T data can be well fitted by the adiabatic small-polaron model: $\rho = AT\exp(E_a/K_BT)$, yielding an activation energy $E_a = 29.71 \pm 0.05$ meV. Figure 6(b) depicts the filed-dependent magnetoresistance: $MR = 100\% \times (\rho(H) - \rho(0))/\rho(0)]$ at selected temperatures. Positive MR at 60 K and 100 K arises from the normal MR effect: the carriers subjected to the Lorentz force in the magnetic field deviate from the original trajectory, increasing the probability of electron collision and causing additional scattering effect, thus increasing the resistance and producing positive MR. At 5 K, negative MR effect emerges, resembling the MR behavior of $CaCu_3Fe_2Ru_2O_{12}$.[47] The negative MR effect can be ascribed to weak localization effect caused by the interference of electron wave functions in disordered media.[48] This effect is usually related to the spin of magnetic ions and influenced by magnetic fields.[49] The negative MR is influenced by the modulation of the external magnetic field on the spin alignment of Fe^{3+}. Theoretical analysis shows that the suppression of spin scattering induced by magnetic field may dominate the negative MR effect. In addition, the MR at 5 K shows a butterfly-shaped hysteresis loop. It is noted that the field in MR maximum coincides with that in M^2–H curve at 5 K (Fig. 6(c)). This phenomenon is similar to the spin-related tunneling effect in Sr_2FeReO_6, where conduction electrons traverse grain/domain boundaries.[50]

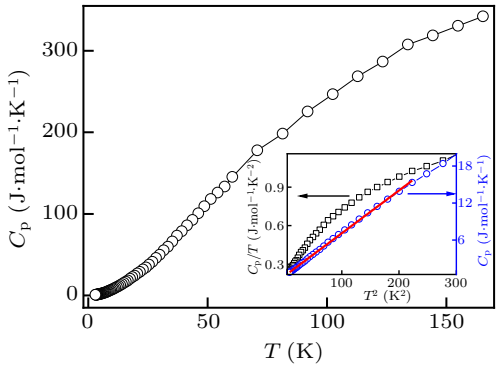


Fig. 7. The specific heat as a function of the temperature for $CeCu_3Fe_2Ru_2O_{12}$. The inset shows that C_p versus T^2 and C_p versus T^3 plot at low-temperature.

The heat capacity (C_p) was measured to elucidate the magnetic and transport characteristics of CeCFRO. As shown in Fig. 7, no anomalies were observed in the specific heat data. It is worth noting that C_p exhibits a T^2 dependence rather than the conventional T^3 behavior at low temperatures (inset of Fig. 7). Typically, the heat capacity at low temperatures follows the relation: $C_p = \gamma T + \beta T^3$, where the T term arises from the contribution of free electrons and the T^3 term originates from the contribution of phonons. However, the T^2 term is rarely observed. This deviation may arise from two possible mechanisms: classical antiferromagnetic spin wave excitation in the two-dimensional system or the opening of the finite energy gap in the excitation spectrum.[51] Recent studies reported T^2-dependent specific heat in spin-frustrated compounds. For example, the specific heat in the Kagomé lattice compound $SrCr_9Ga_3O_{19}$ follows a T^2 law.[52] Although its magnetic susceptibility exhibits spin glass behavior, the T^2 dependence of specific heat challenges the theoretical framework of spin glasses. Moreover, the specific heat of $SrCr_9Ga_3O_{19}$

is almost independent of external magnetic fields,[53] suggesting many-body singlet excitations in its low-energy excitation spectrum.[54] Similar behavior is observed in two-dimensional triangular-lattice compound $NiGa_2S_4$, where only short-range magnetic order exists in its magnetic ground state.[55] Recent work attributes this field-independent T^2 behavior to the spin wave excitation of spiral spin structure.[56] A comparable T^2 dependence behavior in the specific heat has been reported in $CaCu_3Ti_{4-x}Ru_xO_{12}$ ($x = 0.5$), where Ru substitution for Ti leads to the formation of a finite energy gap in the excitation spectrum of the compound. This energy gap suppresses the traditional phonon-dominated T^3 behavior and changes the mode of low-energy excitation.[51]

4. Conclusion and perspectives

A novel *A*-site-ordered perovskite oxide, $CeCu_3Fe_2Ru_2O_{12}$, was synthesized under high-pressure conditions (10 GPa and 1400 K). The compound crystallizes in a cubic crystal structure with space group $Im\bar{3}$, with ordered Ce and Cu ions in a ratio of 1:3 and disordered distribution of Fe and Ru ions at the *B* site. BVS calculations and XPS results confirm the charge configuration in the form of $Ce^{4+}Cu_3^{2+}Fe_2^{3+}Ru_2^{4.25+}O_{12}$. Magnetic measurements reveal a ferrimagnetic transition at $T_C \sim 73.6$ K followed by a spin glass behavior occurs at 50.3 K, consistent with the conventional dynamical scaling model. The resistivity of $CeCu_3Fe_2Ru_2O_{12}$ follows the adiabatic small polaron model. The specific heat at low temperatures shows T^2 dependence arising from the formation of a finite energy gap in the excitation spectrum.

Acknowledgements

Project supported by the National Key Research and Development Program of China (Grant No. 2017YFA0403502) and the Joint Funds of the National Natural Science Foundation of China and the Chinese Academy of Sciences' Large-Scale Scientific Facility (Grant No. U1832115).

References

[1] Shimakawa Y and Mizumaki M 2014 *J. Phys.: Condens. Matter* **26** 473203
[2] Long YW 2016 *Chin. Phys. B* **25** 078108
[3] Zhou L, Dai J H, Chai Y S, Zhang H M, Dong S, Cao H B, Calder S, Yin Y Y, Wang X, Shen X D, Liu Z H, Saito T, Shimakawa Y, Hojo H, Ikuhara Y, Azuma M, Hu Z W, Sun Y, Jin C Q and Long Y W 2017 *Adv. Mater.* **29** 1703435
[4] Long Y W, Hayashi N, Saito T, Azuma M, Muranaka S and Shimakawa Y 2009 *Nature* **458** 60
[5] Long Y W, Saito T, Tohyama T, Oka K, Azuma M and Shimakawa Y 2009 *Inorg. Chem.* **48** 8489
[6] Long Y W and Shimakawa Y 2010 *New J. Phys.* **12** 063029
[7] Yamada I, Shiro K, Etani H, Marukawa S, Hayashi N, Mizumaki M, Kusano Y, Ueda S, Abe H and Irifune T 2014 *Inorg. Chem.* **53** 10563
[8] Shimakawa Y 2015 *J. Phys. D: Appl. Phys.* **48** 504006
[9] Yamada I, Takata K, Hayashi N, Shinohara S, Azuma M, Mori S, Muranaka S, Shimakawa Y and Takano M 2008 *Angew. Chem. Int. Ed.* **47** 7032
[10] Sun N, Li W B, Qin Y, Zheng Z C, Zhang B W, Dong X J, Wei P, Zhang Y X, He X, Xie X Y, Huang K, Wu L L, Lei M, Gou H Y, Yu R Z and Long YW 2024 *Chin. Phys. B* **33** 128101
[11] Shimakawa Y and Takano M 2009 *Z. Anorg. Allg. Chem.* **635** 1882
[12] Etter M, Isobe M, Sakurai H, Yaresko A, Dinnebier R E and Takagi H 2018 *Phys. Rev. B* **97** 195111
[13] Etani H, Yamada I, Ohgushi K, Hayashi N, Kusano Y, Mizumaki M, Kim J, Tsuji N, Takahashi R, Nishiyama N, Inoue T, Irifune T and Takano M 2013 *J. Am. Chem. Soc.* **135** 6100
[14] Zeng Z, Greenblatt M, Subramanian M A and Croft M 1999 *Phys. Rev. Lett.* **82** 3164
[15] Alonso J A, Sanchez-Benitez J, De Andres A, Martinez-Lope M J, Casais M T and Martinez J L 2003 *Appl. Phys. Lett.* **83** 2623
[16] Takata K, Yamada I, Azuma M, Takano M and Shimakawa Y 2007 *Phys. Rev. B* **76** 024429
[17] Homes C C, Vogt T, Shapiro S M, Wakimoto S and Ramirez A P 2001 *Science* **293** 673
[18] Adams T B, Sinclair D C and West A R 2002 *Adv. Mater.* **14** 1321
[19] Yamada I, Tsuchida K, Ohgushi K, Hayashi N, Kim J, Tsuji N, Takahashi R, Matsushita M, Nishiyama N, Inoue T, Irifune T, Kato K, Takata M and Takano M 2011 *Angew. Chem. Int. Ed.* **50** 6579
[20] Kobayashi W, Terasaki I, Takeya J, Tsukada I and Ando Y 2004 *J. Phys. Soc. Jpn.* **73** 2373
[21] Cheng J G, Zhou J S, Yang Y F, Zhou H D, Matsubayashi K, Uwatoko Y, MacDonald A and Goodenough J B 2013 *Phys. Rev. Lett.* **111** 176403
[22] Wang X, Liu M, Shen X D, Liu Z H, Hu Z W, Chen K, Ohresser P, Nataf L, Baudelet F, Lin H J, Chen C T, Soo Y L, Yang Y F, Jin C Q and Long Y W 2019 *Inorg. Chem.* **58** 320
[23] Deng H S, Liu M, Dai J H, Hu Z W, Kuo C Y, Yin Y Y, Yang J Y, Zhao Q, Xu Y J, Fu Z M, Cai J W, Guo H Z, Jin K J, Pi T W, Soo Y L, Zhou G H, Cheng J G, Chen K, Tjeng L H, Jin C Q, Yang Y F and Long Y W 2016 *Phys. Rev. B* **94** 024414
[24] Wang X, Liu Z H, Ye X B, Zhou L, Shen X D, Chen K, Nataf L, Baudelet F, Lin H J, Chen C T, Tanaka A, Weng S C and Long Y W 2021 *Inorg. Chem.* **60** 6298
[25] Chen W T, Mizumaki M, Seki H, Senn M S, Saito T, Kan D, Attfield J P and Shimakawa Y 2014 *Nat. Commun.* **5** 3909
[26] Liu Z H, Zhang S K, Wang X, *et al.* 2022 *Adv. Mater.* **34** 2200626
[27] Liu Z H, Wang X, Ye X B, *et al.* 2021 *Phys. Rev. B* **103** 014414
[28] Liu Z H, Sun Q, Ye X B, *et al.* 2020 *Appl. Phys. Lett.* **117** 152402
[29] Byeon S H, Lee S S, Parise J B and Woodward P M 2006 *Chem. Mater.* **18** 3873
[30] Brown I D and Altermatt D 1985 *Acta Crystallogr. Sect. B: Struct. Sci.* **41** 244
[31] Roulhac P L and Palenik G J 2003 *Inorg. Chem.* **42** 118
[32] Passacantando M and Santucci S 2013 *J. Nanopart. Res.* **15** 1785
[33] Yue Q, Shao B, Shao H Y, Yang F, Wang J H, Wang Y and Liu J H 2020 *J. Mater. Sci.* **55** 8421
[34] Li H, Chen Y, Ma Q, Wang J, Chen Q, Wang G, Wang Y and Wang P 2018 *Mater. Lett.* **216** 199
[35] Lü M F, Deng X L, Waerenborgh J C, Wu X J and Meng J 2014 *J. Solid State Chem.* **211** 1
[36] Chen W T, Mizumaki M, Saito T and Shimakawa Y 2013 *Dalton Trans.* **42** 10116
[37] Senn M S, Chen W T, Saito T, García-Martín S, Attfield J P and Shimakawa Y 2014 *Chem. Mater.* **26** 4832
[38] Deng J M, Han F F, Schwarz B, Knapp M, Ehrenberg H, Hua W B, Hinterstein M, Li G B, He Y, Wang J, Yuan Y and Liu L J 2021 *Inorg. Chem.* **60** 6999
[39] de Almeida J R L and Thouless D J 1978 *J. Phys. A* **11** 983

[40] Kawasaki T, Kawasaki K, Tanaka M and Tomita K 1963 *Prog. Theor. Phys.* **30** 729

[41] Srinivasan G and Seehra M S 1983 *Phys. Rev. B* **28** 6542

[42] Mydosh J A 1993 *Spin Glasses: An Experimental Introduction* (London: Taylor and Francis)

[43] Mydosh J A 2015 *Rep. Prog. Phys.* **78** 052501

[44] Binder K and Young A P 1986 *Rev. Mod. Phys.* **58** 801

[45] Hohenberg P C and Halperin B I 1977 *Rev. Mod. Phys.* **49** 435

[46] Ye X B, Liu Z H, Wang W P, *et al.* 2020 *J. Phys.: Condens. Matter* **32** 075701

[47] Li S M, Pan C B, Zhao G C, *et al.* 2023 *J. Magn. Magn. Mater.* **588** 171366

[48] Beenakker C W J 1997 *Rev. Mod. Phys.* **69** 731

[49] Andrearczyk T, Jaroszynski J, Grabecki G, *et al.* 2005 *Phys. Rev. B* **72** 121309

[50] Kobayashi K I, Kimura T, Tomioka Y, Sawada H and Terakura K 1999 *Phys. Rev. B* **59** 11159

[51] Tsukada I, Kammuri R, Kida T, Yoshii S, Takeuchi T, Hagiwara M, Iwakawa M, Kobayashi W and Terasaki I 2009 *Phys. Rev. B* **79** 054430

[52] Ramirez A P, Espinosa G P and Cooper A S 1990 *Phys. Rev. Lett.* **64** 2070

[53] Ramirez A P, Hessen B and Winklemann M 2000 *Phys. Rev. Lett.* **84** 2957

[54] Sindzingre P, Misguich G, Lhuillier C, Bernu B, Pierre L, Waldtmann C and Everts H U 2000 *Phys. Rev. Lett.* **84** 2953

[55] Nakatsuji S, Nambu Y, Tonomura H, Sakai O, Jonas S, Broholm C, Tsnuetsugu H, Qiu Y and Maeno Y 2005 *Science* **309** 1697

[56] Yamaguchi H, Kimura S, Hagiwara M, Nambu Y, Nakatsuji S, Maeno Y and Kindo K 2008 *Phys. Rev. B* **78** 180404